Statistics and Its Interface Volume 12 (2019) 283–293

Incorporating deep features in the analysis of tissue microarray images

Donghui Yan*, Timothy Randolph, Jian Zou, and Peng Gong*

Tissue microarray (TMA) images have been used increasingly often in cancer studies and the validation of biomarkers. TACOMA—a cutting-edge automatic scoring algorithm for TMA images—is comparable to pathologists in terms of accuracy and repeatability. Here we consider how this algorithm may be further improved. Inspired by the recent success of deep learning, we propose to incorporate representations learnable through computation. We explore representations of a group nature through unsupervised learning, e.g., hierarchical clustering and recursive space partition. Information carried by clustering or spatial partitioning may be more concrete than the labels when the data are heterogeneous, or could help when the labels are noisy. The use of such information could be viewed as regularization in model fitting. It is motivated by major challenges in TMA image scoring—heterogeneity and label noise, and the *cluster* assumption in semi-supervised learning. Using this information on TMA images of breast cancer, we have reduced the error rate of TACOMA by about 6%. Further simulations on synthetic data provide insights on when such representations would likely help. Although we focus on TMAs, learnable representations of this type are expected to be applicable in other settings.

AMS 2000 subject classifications: Primary 62P10.
Keywords and phrases: Tissue microarray images, Automatic scoring, Hierarchical clustering, Recursive space partitioning, Deep representation learning.

1. INTRODUCTION

The tissue microarray (TMA) technology was developed during the last three decades [10, 42, 58] as a high-throughput technology for the evaluation of histology-based laboratory tests. A particularly desirable feature of TMAs is that they allow the immunohistochemical (IHC) staining of hundreds of sections all at once, thus standardizing many variables involved. A TMA slide is an array of hundreds of thin tissue sections cut from small-core biopsies (less than 1 mm in diameter). Such biopsies are taken from cell lines, or archives of frozen or formalin-fixed paraffin-embedded tissues. These arrayed sections are then stained and mounted on a TMA slide, which will be viewed with a high-resolution microscope. A TMA image is produced from each tissue section. Figure 1 is an illustration of the TMA technology.

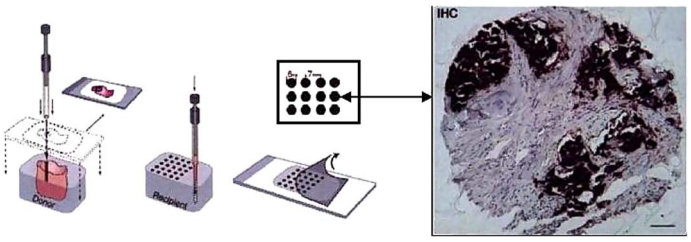

Figure 1. An illustration of the TMA technology (the left half of the image was taken from [64]). Small tissue cores are first extracted from tumor blocks, and stored in archives which are frozen or preserved with formalin. Then thin slices of tissues are sectioned from the tissue core. A tissue slide is formed by an array of hundreds of tissue sections (possibly from different patients). Biomarkers are then applied to the tissue sections (which then typically show darker colors). A TMA image is then captured for each tissue section from a high-resolution microscope.

A standard approach to quantify the qualitative IHC readings is for a pathologist to provide a single-number score to each spot which summarizes the pattern of staining as it relates to specific types of cells. For example, a protein marker that is highly expressed in cancerous cells will exhibit a qualitatively different pattern than a marker that is less indicative of cancer and may exhibit non-specific staining. These scores serve as a convenient proxy to study the tissue images, given the complexity (staining patterns are not localized in positions, shape or size) and potential high dimensionality of tissue images (a TMA image typically has a size of 1504×1440 pixels). They have been used for a wide array of applications, including the validation of biomarkers, assessment of therapeutic targets, analysis of clinical outcome [32], tumor progression analysis [2], and the study of genomics and proteomics ("imaging genetics") [34]. The use of TMAs in cancer biology has increased dramatically in recent years [10, 25, 32, 55]. Particularly, since TMAs allow the rapid assessment of DNA, RNA and protein expression on large tissue samples, they are emerging as the standard tool for the validation of diagnostic and prognostic biomarkers [32].

*Joint corresponding authors.

The inherent variability and subjectivity with manual scoring [4, 5, 10, 15, 20, 25, 38, 52, 56, 57] of TMA images, as well as the demand for reproducible large-scale high-throughput call for the automatic scoring of TMA images. A number of commercial tools have been developed, including ACIS (ChromaVision Medical Systems), Ariol (Applied Imaging), TMAx (Beecher Instruments) and TMALab II (Aperio) for IHC, and the AQUA method [9] (HistRx, Inc.) for fluorescent labeled images. However, most are difficult to tune and the resulting models are sensitive to many variables such as IHC staining quality, background antibody binding, hematoxylin counterstaining, and the color and hue of chromogenic reaction products used to detect antibody binding.

This work extends TACOMA—an automatic scoring algorithm for tissue images that is robust against various factors such as variability in the image intensity and staining patterns etc [64]. While TACOMA achieves a scoring accuracy comparable to a trained pathologist on a number of tumor and biomarker combinations [64], naturally, one would wonder if it is possible to make further progress. One source of inspiration comes from the recent advance in deep learning [35, 44], especially in the area of image classification [43, 50, 51]. For TMA images, however, the huge training set required by deep neural networks, typically at the magnitude of millions, is hard to obtain in reality (techniques such as transfer learning [53] may help, but still it is not easy to get large enough training sample). In a typical TMA database, for example, the Stanford TMAD database [48], the size of the training set associated with any particular biomarker is merely in the order of hundreds.

There are several factors that would limit the availability of TMA images. While natural images—the type of images that deep learning has had huge success on—or their labels can be easily acquired by web scraping or crowd-sourcing, it is much harder for TMA images which have to be acquired from human body and captured by high-resolution microscopes and high-end imaging devices. Moreover, the labelling of TMA images is typically done by pathologists. In terms of classification, the natural and TMA images are of a completely different nature. A natural image typically consists of a small number of well-defined objects, which form important high-level features for image categorization. In contrast, the scoring of TMA images is not about how the staining pattern looks like, rather the "severity and spread" of the pattern matters, i.e., it concerns some global property and requires considerable expertise. The sample size is further limited by the fact that TMA images are scored by biomarkers or cancer types; there are over 100 cancer types according to the US National Cancer Institute [54].

What lesson can we learn from deep learning? Rather than a tool for building a powerful classifier with deep layers of neural networks, we view the essence of deep learning as a way of finding a suitable representation (possibly hierarchical) for the underlying problem through computation. Such a representation would otherwise be hidden from manual feature engineering.

In particular, we are able to use unsupervised learning to find features of a group nature, which along with existing features used by TACOMA, leads to improved performance in scoring. This was motivated by known major challenges in the scoring of TMA images—heterogeneity and label noise, and inspired by the *cluster* assumption in semi-supervised learning [14, 66]. As such new features are typically beyond usual feature engineering and had to be found by computation, we term those deep features; of course by "deep" also means we had inspirations from deep learning and the new features are produced from existing features. For this reason and due to the intimate connection of our approach to TACOMA, we term our approach *deepTacoma*.

The organization of the remainder of this paper is as follows. We describe the TACOMA algorithm in Section 2. In Section 3 we discuss our method and some new classes of feature representations. In Section 4, we present our experiments and results. We conclude with Section 5.

2. THE TACOMA ALGORITHM

In this section, we will briefly describe the TACOMA algorithm. This will provide a basis to understand *deepTacoma* which extends upon TACOMA. To ensure consistency in notations, we begin with an introduction of notations following [60, 64]. Note that the scoring systems [48] adopted in practice typically use a small number of discrete values, such as $\{0, 1, 2, 3\}$, as the *score* (or *label*) for TMA images. We formulate the scoring of TMA images as a classification problem, following [64].

The primary challenge in TMA image analysis is the lack of easily-quantified criteria for scoring: features of interest are not localized in position, shape or size. There are no "landmarks" and no hope of "image registration" for comparing features. Rather, this problem is truly a challenge about quantifying *qualitative* properties of the TMA images. The key insight that underlies TACOMA is that in spite of heterogeneity, TMA images exhibit strong statistical regularity in the form of visually observable textures or *staining patterns*. In TACOMA, such patterns are captured by an important image statistics—the gray level co-occurrence matrix (GLCM).

2.1 The gray level co-occurrence matrix

The GLCM of an image is a matrix of counting statistics about the spatial pattern of neighboring pixels. It can be crudely viewed as a "histogram" according to a certain spatial relationship. It was proposed by Haralick [30] and has been proven successful in a variety of applications [26, 30, 46, 64]. The GLCM is defined with respect to a particular spatial relationship described below.

Definition [60, 64]. The spatial relationship between a pair of pixels in image I involves their relative position and spatial distance. The set $\Re$ of spatial relationships of interest

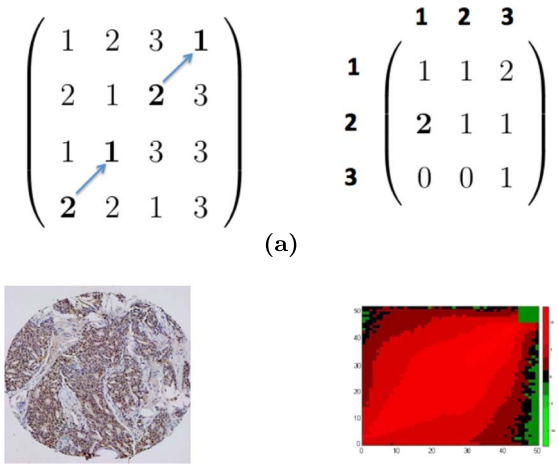

(a)

(b)

Figure 2. Example images and GLCMs. (a) A toy image and its GLCM. The toy image is a 4×4 image with a 3×3 GLCM for $\sim = (\nearrow, 1)$. (b) A TMA image (left panel) and the heatmap of its GLCM (right panel, in log scale, and taken from [64]). In the right panel, the axis labels (0-50) indicate the normalized pixel values in a TMA image; the color (scale indicated by a color bar) of the heatmap represents the value of entries in the GLCM.

is defined as

$$\Re = D \otimes L = \{\nearrow, \ \searrow, \ \nwarrow, \ \swarrow, \ \downarrow, \ \uparrow, \ \rightarrow, \ \leftarrow\} \otimes \{1, ..., d\}$$

where D is the set of possible directions, and L is the distance between the pair of pixels along the direction.

Definition [60, 64]. For a given spatial relationship $\sim \in \Re$, the GLCM for an image (or a patch) is defined as (assume the number of gray levels in the image is N_g)

> A $N_g \times N_g$ matrix such that its (a, b)-entry counts the number of times two pixels, $P_1 \sim P_2$, and their gray values are a and b, respectively, for $a, b \in \{1, 2, ..., N_g\}$.

Note that, an image can have multiple GLCMs, with each corresponding to a particular spatial relationship. The definition of GLCM is illustrated in Figure 2 with a toy and a real TMA image (taken from [64]). For a good balance of computational efficiency and discriminative power, we take $N_g = 51$ and apply uniform quantization [28] over the 256 gray levels in our application.

2.2 An algorithmic description of TACOMA

The TACOMA algorithm is particularly simple to describe. First, all TMA images are converted to their GLCM representations. Then the training set (GLCMs and their respective scores) is fed to some training algorithm to obtain a trained classifier. The trained classifier will be applied to get scores for TMA images in the test set. Random Forests (RF) [7] is chosen as the training algorithm due to its exceptional performance in many classification tasks that involve high dimensional data [12].

Algorithm 1 The TACOMA algorithm

1: For each image patch Z_i, compute its GLCM matrix $Z_i^g, i = 1, ..., l$;
2: Build feature mask $\mathcal{M}_i$ as the set of indices for which entries of Z_i^g surpass a threshold τ_i, and set $\mathcal{M} = \cup_{i=1}^{l} \mathcal{M}_i$;
3: **for** $i = 1$ **to** $n + m$ **do**
4: Compute GLCM of image I_i and keep only entries in the index set $\mathcal{M}$;
5: Denote the resulting matrix by X_i;
6: **end for**
7: Feed $\cup_{i=1}^{n}\{(X_i, Y_i)\}$ to RF to obtain a classification rule $\hat{f}$;
8: Apply $\hat{f}$ to X_i to obtain score for image $I_i, i = n+1, ..., n+m$.

Denote the training sample by $(I_1, Y_1), ..., (I_n, Y_n)$ where I_i's are images and Y_i's are scores (thus $Y_i \in \{0, 1, 2, 3\}$). Let $I_{n+1}, ..., I_{n+m}$ be new TMA images that one wish to score (i.e., the test set has a size of m). Additionally, let $Z_1, ..., Z_l$ denote the small set of 'representative' image patches; $l = 5$ in TACOMA [64]. TACOMA is described as Algorithm 1. Here τ_i is a threshold value used to filter unimportant features. In particular, we set it to be the median of all entries in GLCM matrix Z_i^g for $i = 1, ..., l$. Steps 1-2 are optional; these are used to create a *mask* through which all GLCMs are filtered. The mask is created from a small number TMA image patches selected by pathologists that would reflect important aspects when they manually score the images. This is where the pathologists could incorporate their domain expertise in the TACOMA algorithm. In this work, however, we will not include masking due to the lack of pathologists for the verification of representative image patches; it is included in the description mainly to be consistent with how TACOMA was described in [64].

3. THE DEEPTACOMA METHOD

The main idea of our method is to look for some "good" representation of the TMA images for the purpose of scoring. Here "good" means such a representation can lead to information beyond the straightforward use of GLCM features. This is essentially a feature engineering problem (see, for example, [29]), and there are many possibilities one could explore. Our strategy is to look for those representations of a group nature which reflects how close data points are to each other. This is motivated by practical success of the *cluster* assumption in semi-supervised learning [14, 66], as well as known major challenges in developing scoring algorithms for TMA images—heterogeneity and label noise. Alternatively, one may consider using regularized mixture models proposed recently by Gao and his coauthors [24] to deal with those challenges, but that is beyond the scope of the present work. Our approach is really a problem-driven approach—we directly target at those specific known challenges and

seek representations that are informative towards them. Our approach is implemented as two classes of features, one generated from clustering (including K-means and hierarchical clustering) and the other based on recursive space partition.

The representations we explore are a group property that relates different data points and is beyond what may be revealed by features of individual data points alone. Therefore we expect such representations would lead to additional information that may help in the scoring of TMA images. One may argue that the label (or score) along with the TMA images would have already captured such information. We note, however, that TMA images receiving the same score could still be highly heterogeneous. Thus, information carried by clustering or space partition may be more concrete than that by the labels. Heterogeneity is itself, in certain sense, a group property. Including those features related to grouping may help in directing the algorithm to build sub-models to deal with heterogeneous data as appropriate. Moreover, TMA labels are typically noisy. Different pathologists may score differently, and the same pathologist may give different scores to the same image at different scoring sessions [64]. The information carried by clustering or space partition would likely help against label noise, in a similar way as the *cluster* assumption in semi-supervised learning would do to compensate the scarcity of labeled instances: many data instances do not have a label, and information from those labeled instances could be borrowed through the group property. One could view the information revealed by clustering or space partition as a type of regularization in model fitting. Thus either a more stable model, or a model with better accuracy, would be expected.

The deep features, together with the original features, form the augmented features. This will be the input to a classification algorithm (RF in our case). Figure 3 is an illustration of how this is done. For clustering-based deep features, we use the cluster ID as the deep features. To obtain a more informative set of deep features, in the case of hierarchical clustering, we generate the dendrogram first and then cut it at many different heights. Each height will lead to a different clustering of the data. The IDs obtained from clustering at all different heights form the set of deep features. For recursive space partition, we implement by an ensemble of random projection trees (rpTrees) [18] (i.e., random projection forests [65]). Many rpTrees are generated, and the leaf node IDs from each tree form a deep feature. Instead of the tree leaf node IDs, we also attempt to encode the path from the root node to each leaf node, but that is less effective.

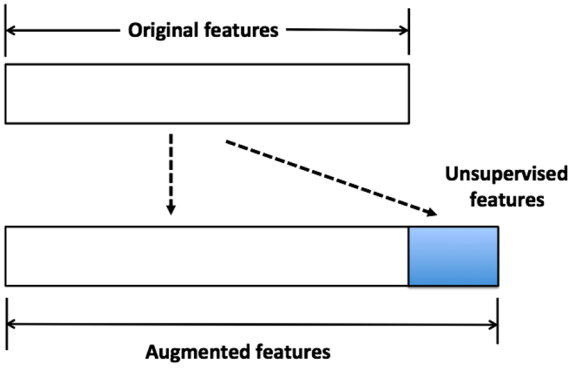

Figure 3. Illustration of deep features. The unsupervised features (or deep features) are generated from the original features, which together form the augmented features to be used for classification tasks.

For the rest of this section, we will briefly describe K-means clustering, hierarchical clustering, and rpTrees.

3.1 K-means clustering

K-means clustering was developed by S. Lloyd in 1957 (but published later in 1982) [47], and remains one of the simplest yet most popular clustering algorithms. The goal of K-means clustering is to split data into K partitions (clusters) and assign each point to the "nearest" cluster (mean). A cluster mean is the center of mass of all points in a cluster, or the arithmetic mean of all points in a cluster; it is also called *cluster centroid or prototype*. The algorithm is very simple. Starting with a set of randomly selected cluster centers, the algorithm alternates between two steps: assign all the points to its nearest cluster centers, and recalculate the new cluster centers, and stops when no further changes are observed on the cluster centers.

For a more detailed description of K-means clustering, please refer to the appendix (c.f., Section A.1) or [31, 47].

3.2 Hierarchical clustering

Hierarchical clustering refers to a class of clustering algorithms that first organize the data in a hierarchy (called *dendrogram*), and then form clusters by cutting through the dendrogram at a certain height. Depends on how the hierarchy is formed, bottom up or top down, there are two types of hierarchical clustering approaches, agglomerative or divisive clustering. In the following, we will briefly describe them.

Agglomerative clustering is a bottom-up approach. It starts by treating each data point as a singleton cluster (i.e., a cluster that contains only one data point). Two points (or clusters) that are the most similar are fused to form a bigger cluster. Then points or clusters are continually fused one-by-one in order of highest similarity or cluster to which they are most similar. Eventually, all points are merged to form a single "giant" cluster. This produces a dendrogram to be cut through at a certain height to form clusters.

Divisive clustering takes a top-down approach. Initially, all data points belong to the same cluster. Then, recursively, clusters are divided until each cluster contains only one data point. At each stage, the cluster with largest diameter (defined as the largest dissimilarity between any two points in a cluster) is selected for further division. To divide the

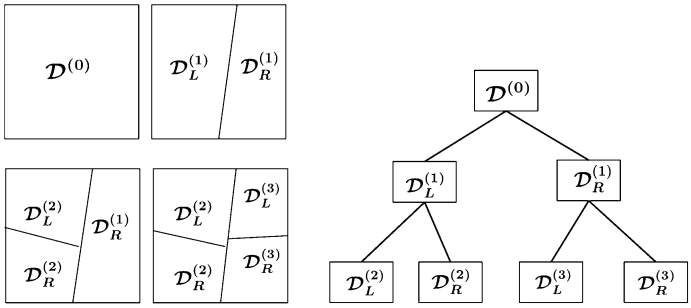

Figure 4. Illustration of space partition and random projection trees. The superscripts indicate the order of tree node split. One starts with the root node, $\mathcal{D}^{(0)}$, which corresponds to all the data. After the first split, $\mathcal{D}^{(0)}$ is partitioned into its two child nodes, $\{\mathcal{D}_L^{(1)}, \mathcal{D}_R^{(1)}\}$. The second split partitions the left child node, $\mathcal{D}_L^{(1)}$, into its two child nodes, $\{\mathcal{D}_L^{(2)}, \mathcal{D}_R^{(2)}\}$. The third split would be on node $\mathcal{D}_R^{(1)}$ which leads to two new child nodes, $\{\mathcal{D}_L^{(3)}, \mathcal{D}_R^{(3)}\}$. This process continues until a stopping criterion is met.

selected cluster, one looks for its most disparate observations (the point with largest average dissimilarity to others), which initiates the so-called "splinter group", then re-assign data points closer to the"splinter group" as one group and the rest as another group. The selected cluster is split into two smaller new clusters.

For more details about hierarchical clustering, please refer to [33, 41, 59].

3.3 Recursive space partition

Another type of representation is based on recursive space partition. It is a class of methods widely used in many applications [23, 39, 62, 63] that organizes the data points according to their proximity in a recursive fashion. The recursive space partition is typically implemented with a popular data structure, the k-d tree [3]. We use its randomized version, rpTrees [18]. One advantage of rpTrees over kd-tree is its ability to adapt to the geometry of the underlying data and readily overcomes the curse of dimensionality, according to [18]. The rpTrees starts with the entire data set, $\mathcal{D}^{(0)}$, as the root node. The split on the root node results in two child nodes, on each of which the same splitting procedure applies recursively until some stopping criterion is met. For example, the node becomes too small (i.e., contains two few data points). Data points falling into the same leaf node will be 'similar' to each other. An illustration of recursive space partition via a tree is shown in Figure 4.

The algorithmic implementation of rpTrees uses a queue, $\mathcal{W}$, of working nodes to implement rpTrees. Initially the queue contains only the root node, D, which corresponds to the given data set. In each iteration, a node is picked from the queue, then split (or no processing if it is smaller than a predefined size, n_s), and the resulting child nodes are pushed into the queue. This process continues until there are no more working nodes in the queue. Let $P_{\vec{r}}(a)$ denote the projection of point a onto line $\vec{r}$. The algorithm will return t, the rpTrees to be built from D. The pseudo code for the algorithm is described as Algorithm 2.

Algorithm 2 *rpTree(D)*

```
Let D be the root node of tree t;
Initialize the set of working nodes W ← {D};
while W is not empty do
    Randomly pick W ∈ W and set W ← W − {W};
    if |W| < n_s then
        Skip to the next round of the while loop;
    end if
    Generate a random line r⃗;
    Project points in W onto r⃗, let M = {P_r⃗(w) : w ∈ W};
    Let a = min(M) and b = max(M);
    Generate a splitting point s uniformly over interval [a, b];
    Split node W by W_L = {a : P_r⃗(a) < s} and W_R = {a :
    P_r⃗(a) ≥ s};
    W.left ← W_L and W.right ← W_R;
    Update the working set by W ← W ∪ {W_L, W_R};
end while
return(t);
```

4. EXPERIMENTS

We conduct experiments on both synthetic data and TMA images. The TMA images are the data that our methods are primarily targeting at. The synthetic data are generated from Gaussian mixtures, and serve the purpose of gaining insights on when our 'deep' features may help. Our approach is motivated by the intuition that features leveraging the group property may be useful when the labels are noisy or when the data are heterogeneous, and we have expressly created simulation scenarios (i.e., Gaussian mixtures $\mathcal{G}_1$ and $\mathcal{G}_2$ in Section 4.1) for these.

For simplicity, we consider 0-1 loss for classification throughout, and use the error rate on the test sample as our performance metric. For K-means clustering, we use the R package *kmeans*, and for hierarchical clustering, we use three different R packages, including *hclust*, *diana*, and *agnes*. For rpTrees, an ensemble of rpTrees (i.e., random projection forests) are generated and each tree corresponds to a new deep feature; we use the R implementation for random projection forests from [65]. The ensemble size is related to the model complexity of the resulting class of classifiers; we can increase the ensemble size when the training sample size increases. RF is chosen as the classifier. According to [64], RF is far superior to support vector machines (SVM) [16] and boosting methods [22] in scoring TMA images. This is likely due to the high data dimension (2601 when using GLCM) and potential label noise in the data. RF has strong built-in capability in feature selection and noise-resistance, while SVM and boosting methods are typically prune to those. This is also supported by related work on the segmentation

of tissue images [36], and many large scale simulation studies [12]. In all our experiments, we fix the number of trees in RF to be 100 (adequate by our experience, and no attempt is made in finding the best number), and the number of tries in selecting variables for node split is chosen from $\{[\sqrt{p}], [2\sqrt{p}]\}$ where p is the number of features in the data. Also for all simulations, a randomly selected half of the data are used for training and the rest for test, and results are averaged over 100 runs.

For the rest of this section, we present details about our experiments on the Gaussian data and the TMA images.

4.1 Gaussian mixtures

Three different Gaussian mixtures, $\mathcal{G}_1, \mathcal{G}_2$ and $\mathcal{G}_3$, are considered. $\mathcal{G}_1$ and $\mathcal{G}_2$ correspond to the usual Gaussian mixture data, and heterogeneous data, respectively, and $\mathcal{G}_3$ uses the covariance matrix estimated from the GLCM matrix of TMA images used in our experiment. Gaussian mixture $\mathcal{G}_1$ is specified as

$$\frac{1}{2}\mathcal{N}(\boldsymbol{\mu}, \Sigma) + \frac{1}{2}\mathcal{N}(-\boldsymbol{\mu}, \Sigma), \tag{1}$$

where '1/2's indicate that half of the data are generated from $\mathcal{N}(\boldsymbol{\mu}, \Sigma)$ and half from $\mathcal{N}(-\boldsymbol{\mu}, \Sigma)$. Here $\mathcal{N}(\boldsymbol{\mu}, \Sigma)$ stands for Gaussian distribution with mean $\boldsymbol{\mu} \in \mathbb{R}^p$ and covariance matrix Σ. We take $p = 40$, and $\boldsymbol{\mu} = (0.3, ..., 0.3)^T$. The covariance matrix Σ is defined such that its (i, j)-entry is given by

$$\Sigma_{ij} = \rho^{|i-j|}, \text{ for } \rho \in \{0.1, 0.3, 0.5\}.$$

If the data is from $\mathcal{N}(\boldsymbol{\mu}, \Sigma)$, then we assign it a class label '1' otherwise a label '2'. The sample size for all of $\mathcal{G}_1, \mathcal{G}_2$ and $\mathcal{G}_3$ are 1000. To see the effect of label noise, we randomly select a proportion of ϵ of the training instances and flip their labels, i.e., change from '1' to '2' or from '2' to '1'.

Our naming convention and experimental settings are as follows. 'RF' indicates results by RF on original Gaussian mixture data or GLCM features for the TMA images only (term these as original data in the following); 'hClustering' for results by RF on original data augmented by features derived from hierarchical clustering; 'rpTrees' for results by RF on original data augmented by features derived from rpTrees; 'K-means' for results by RF on original data augmented by features derived from K-means clustering. Such a convention is followed throughout our experiments. For K-means clustering, the best results are reported when the number of clusters varies from $\{30, 40, ..., 120\}$. For hierarchical clustering, the number of clusters ranges from $[10, 60]$ and all three different hierarchical clustering procedures are used. Note that here clustering is used as a tool to extract latent structures from the data by grouping similar or nearby data points, the exact number of clusters is no longer as important as in the usual clustering setting. The main goal is to ensure that the grouping is fine "enough", and meanwhile each group has a sufficient number of data points. The same applies to recursive space partitions. For rpTrees, we try different ensemble size in the set $\{200, 400, 600, 800\}$, and find the difference small with 800 doing slightly better; no attempt is made in obtaining the best results. The maximum size of a node is fixed at 20. The experimental results are summarized in Table 1.

Table 1. Error rates on Gaussian mixture $\mathcal{G}_1$

ρ	ϵ	**RF**	**K-means**	**hClustering**	**rpTrees**
0.1	0	8.18%	7.68%	5.16%	5.82%
	0.1	9.25%	8.90%	5.52%	6.32%
	0.2	11.16%	10.71%	6.91%	8.06%
	0.3	15.28%	15.04%	11.21%	12.25%
0.3	0	11.55%	11.08%	9.26%	9.51%
	0.1	12.32%	12.16%	9.68%	9.98%
	0.2	13.77%	13.53%	11.15%	11.61%
	0.3	18.09%	17.69%	16.17%	15.58%
0.5	0	15.81%	15.73%	14.47%	14.38%
	0.1	16.73%	16.44%	15.43%	14.97%
	0.2	17.83%	17.56%	17.09%	16.43%
	0.3	22.17%	21.87%	21.98%	19.88%

It can be seen from Table 1 that, in all cases, both the hierarchical clustering and the rpTrees based approaches lead to reduced error rates while the gain by K-means clustering is marginal (indicating that more refined structural information may be required). Moreover, when the label noise is moderate, for example when $\epsilon = 0.1$, the reduction in error rate is often more significant than other cases (including the case without label noise, i.e., $\epsilon = 0$). When ρ is small, that is, individual features in the data are less correlated, deep features tend to lead to more substantial improvement in classification performance. This is probably because, in such settings, one can get higher quality unsupervised features (as a result of better clustering or space partitions).

Gaussian mixtures $\mathcal{G}_2$ is specified as

$$\frac{1}{4}\mathcal{N}(\boldsymbol{\mu_1}, \Sigma) + \frac{1}{4}\mathcal{N}(\boldsymbol{\mu_2}, \Sigma) + \frac{1}{4}\mathcal{N}(-\boldsymbol{\mu_1}, \Sigma) + \frac{1}{4}\mathcal{N}(-\boldsymbol{\mu_2}, \Sigma),$$

which indicates that a quarter of the data are generated from each of the 4 Gaussians. Same as $\mathcal{G}_1$, we take $p = 40$. The Gaussian mixture centers are fixed as $\boldsymbol{\mu_1} = (0.5, ..., 0.5, 0, ..., 0)^T$ and $\boldsymbol{\mu_2} = (0, ..., 0, 0.5, ..., 0.5)^T$, where for both $\boldsymbol{\mu_1}$ and $\boldsymbol{\mu_2}$, exactly half of the components are 0. The covariance matrices are the same as for $\mathcal{G}_1$. If the data is generated from either $\mathcal{N}(\boldsymbol{\mu_1}, \Sigma)$ or $\mathcal{N}(\boldsymbol{\mu_2}, \Sigma)$, then we assign it a class label '1' otherwise a label '2'. This produces heterogeneous data in the sense that data with the same class label may be from different Gaussians. The results are reported in Table 2 with similar patterns as in Table 1.

Gaussian mixture $\mathcal{G}_3 \in \mathbb{R}^{2601}$ is specified as $\frac{1}{2}\mathcal{N}(-\boldsymbol{\mu}, \Sigma) + \frac{1}{2}\mathcal{N}(\boldsymbol{\mu}, \Sigma)$, where Σ is estimated from the GLCM of all TMA images used in our experiment. Table 3 shows the error rate by RF and that with additional features generated by K-means clustering, hierarchical clustering, and rpTrees, respectively. While deep features by K-means clustering barely

Table 2. Error rates on Gaussian mixtures $\mathcal{G}_2$

ρ	ϵ	RF	K-means	hClustering	rpTrees
0.1	0	12.69%	12.45%	9.89%	10.36%
	0.1	13.64%	13.55%	10.50%	11.53%
	0.2	15.63%	15.42%	12.38%	13.40%
	0.3	20.53%	20.18%	17.37%	18.48%
0.3	0	15.69%	15.91%	14.11%	14.14%
	0.1	17.28%	16.79%	14.95%	15.22%
	0.2	18.76%	18.61%	16.67%	16.95%
	0.3	23.41%	23.03%	22.39%	21.37%
0.5	0	19.56%	20.49%	19.85%	18.07%
	0.1	20.65%	21.33%	20.50%	19.14%
	0.2	22.63%	23.02%	23.07%	21.08%
	0.3	26.35%	26.67%	26.67%	24.44%

Table 3. Error rates on Gaussian mixture $\mathcal{G}_3$

ϵ	RF	K-means	hClustering	rpTrees
0.1	1.58%	1.48%	1.18%	1.10%
0.2	3.42%	3.24%	3.06%	2.40%
0.3	9.48%	9.12%	8.24%	7.68%
0.4	26.50%	25.70%	26.16%	25.94%

improve the results, those by rpTrees yield notable improvement following a similar pattern as that for $\mathcal{G}_1$ and $\mathcal{G}_2$ (i.e., results improved when the label noise is moderate). Here, K-means or hierarchical clustering probably suffer from the high dimensionality of the data to which rpTrees is more resistant, a desirable property of rpTrees [18].

Note here all Gaussian mixtures $\mathcal{G}_{1-3}$ use a common covariance matrix for their mixture components. In statistics and machine learning, it is not unusual to assume a common covariance matrix for Gaussian mixtures. For example, the liner discriminant analysis (LDA) arises from such an assumption. According to Hastie, Tibshirani and Friedman [33], in terms of decision boundary, the difference between LDA and quadratic discriminant analysis (QDA) is small, and both perform well on an amazingly large and diverse set of classification tasks. In the STATLOG project [49], LDA was among the top three classifiers for 7 of the 22 datasets, QDA among the top three for four datasets. Indeed many published work assume a common covariance matrix for Gaussian mixtures; see, for example, [6, 17, 21, 61].

4.2 Applications on TMA images

The TMA images are taken from the Stanford Tissue Microarray Database, or STMAD (see [48] and http://tma.stanford.edu/). TMAs corresponding to the biomarker, estrogen receptor (ER), for breast cancer tissue are used since ER is a known well-studied biomarker. Each image is assigned a score (i.e., label) from $\{0, 1, 2, 3\}$. The scoring criteria are: '0' indicating a definite negative (no staining of tumor cells), '3' a definitive positive (most cancer cells show dark nucleus staining), '2' for positive (a small portion of tumor cells show staining or a majority show weak staining), and '1' indicates ambiguous weak staining in a small portion of tumor cells, or unacceptable image quality.

Table 4. Error rate in scoring TMA images. Note that the first row corresponds to results obtained by RF on the original set of features (i.e., without deep features)

Deep features	# clusters or leaf nodes	Error rate
—	—	24.79%
K-means	40	24.02%
Diana	[10,40]	24.20%
Agenes	[10,40]	24.14%
hclust	[10,40]	24.29%
Agenes + Diana	[10,40]	23.77%
Agenes + hclust	[10,40]	23.71%
hclust + Diana	[10,40]	23.52%
Agenes + Diana + hclust	[10,40]	**23.46**%
rpTrees	30	**23.28**%

There are totally 695 TMA images for ER in the Stanford database. The GLCM for $(\nearrow, 3)$ is used. Different choices of direction and distance of interaction for spatial relationship were explored in [64], and $(\nearrow, 3)$ shows the greatest discriminating power when ER as a biomarker is used for breast cancer. The pathological interpretation is that, the distance of interaction is related to the size of the staining pattern for the biomarker and cancer type, and the staining pattern is approximately rotationally invariant (thus the choice of direction is not as important). Indeed when more spatial relationships are included or combined, the changes in the results are negligible. The deep features, either by clustering or rpTrees, are obtained for all the images. Then we fit *deepTacoma* on the training set (over the set of augmented features) and apply the fitted classifier to the test set.

We conduct *three sets of experiments* on TMA images, including those on *deepTacoma*, when combining deep features generated by hierarchical clustering and rpTrees, and deep learning with TMA images. These are described in the next three subsections, respectively.

4.2.1 Experiments with *deepTacoma*

The results on *deepTacoma* are reported in Table 4. In the case of hierarchical clustering, the dendrogram is cut such that the number of groups run through $[10, 40]$. Similar as the Gaussian mixture data, the ensemble size for rpTrees is explored from $\{200, 400, 600, 800\}$ and a value of 600 yields similar but slightly better results. An error rate at 24.79% is obtained by RF on the original GLCM features (i.e., without using deep features). The best results are achieved when combining different hierarchical clustering algorithms over a range of different number of clusters, or the ensemble of rpTrees. There is about a 6% reduction in error rates for TMA images of breast cancer, which we consider a notable improvement given that TACOMA algorithm already achieves

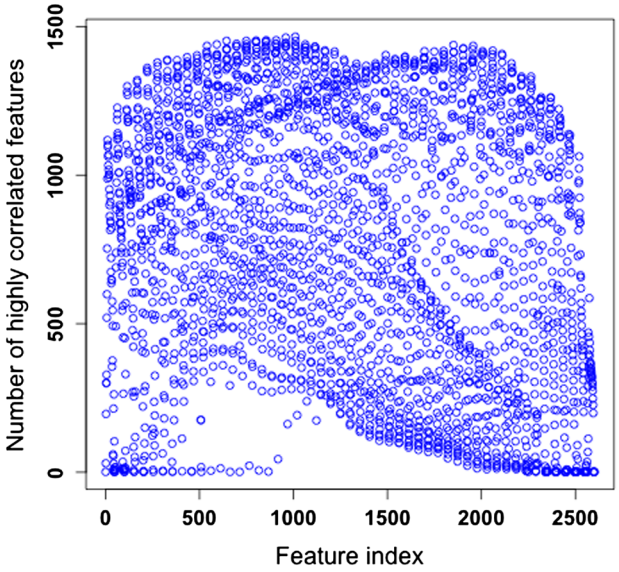

Figure 5. Number of highly correlated features for each of the 2601 image features.

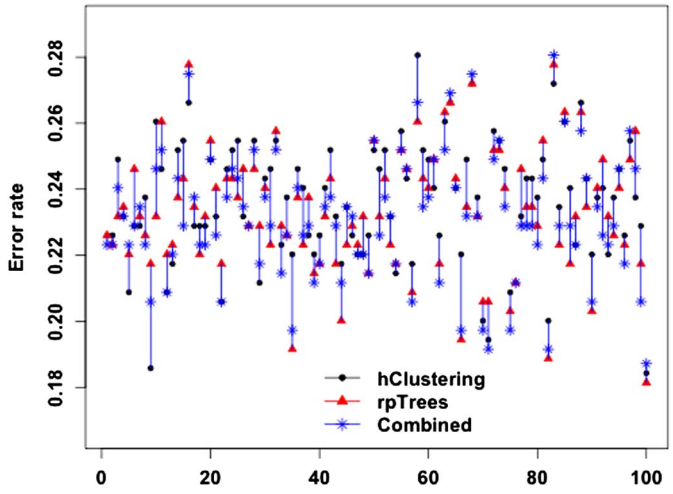

Figure 6. Error rates of RF with deep features by hierarchical clustering, rpTrees, and the combination of the two resulting RF classifiers over 100 runs. For better visualization, the three error rates of the same run (i.e., common training and test set) are connected vertically.

a performance at the level of a trained pathologist and that progress in this field is typically incremental in nature.

One possible reason that we are not able to further improve the performance of *deepTacoma* is probably due to the fact that the image features are highly correlated. According to our simulation on synthetic data (c.f. Table 1 and Table 2), it becomes challenging to use deep features to further improve the performance when the correlation is high. Figure 5 confirms this by showing the number of "highly correlated" features for each of the 2601 features, and for most of the features, such a number would be larger than 500. Here by "highly correlated" we mean the correlation coefficient has its absolute value larger than 0.6. Such a high correlation among features motivates us to carry out a principal component analysis (PCA) [37] of the TMA image data and then apply RF over the leading principal components. Simulations are conducted using from 2 to 100 principal components (for each the results are averaged over 100 runs), which explains up to 99.99% of the total variation in the data. The lowest error rate was 29.28%, achieved at around 50 principal components. This may serve as a further indication on the hardness of scoring TMA images (an algorithm has to detect the hidden nonlinear structures in the data formed by TMA images to score well).

4.2.2 Combining deep features

Given that we have formed deep features by hierarchical clustering and by rpTrees, it is possible to combine these two. We explore two alternatives, leaving many other possibilities to future work. In the first option, all deep features are added to the existing pool of GLCM features and then train the classifier. This leads to an error rate of 23.40%, in between what we get by using deep features separately to train a classifier. This is likely due to the relatively small training sample size as compared to the complexity of the function class for the classifiers when combining features.

In the second option, we train RF classifiers with deep features by hierarchical clustering and by rpTrees *separately*, and then combine the two resulting classifiers. For a given test instance, each of the two classifiers gives a vote in the form of a vector of weights towards 4 classes $\{0, 1, 2, 3\}$; denote the voting vectors by v_1 and v_2, respectively. The two voting vectors are combined by a simple linear combination $v_1 + \beta v_2$; the value of β could be determined by cross validation. The label of the test instance is given by the majority class using the combined votes. As an example, say, $v_1 = (0.38, 0.14, 0.11, 0.37), v_2 = (0.28, 0.08, 0.15, 0.49)$ and $\beta = 1.1$, the combined votes would be $(0.69, 0.23, 0.27, 0.91)$. Individually the two classifiers would report a label '0' and '3', respectively, and the combined votes would report a label of '3'. Reflecting our belief that the classifier with deep features by rpTrees is slightly stronger, we set $\beta = 1.1$. This leads to an error rate of 23.16%, marginally improving over 23.28%. The gain is small. However, if we watch over individual runs, the result is actually fairly encouraging—the combined classifier has an error rate either close to or smaller than the best of the two in most runs. Figure 6 is a scatter plot of the test set error rates by each of the two classifiers, and their combination over 100 runs.

4.2.3 Experiments with deep learning

Given the popularity of deep learning, we also carry out simulations on TMA images with deep neural networks. For an overview of deep neural network, please refer to [27]. The

Table 5. Error rate on TMA images of different sizes by deep learning and RF

Image size	Deep neural network	RF
16×16	34.92%	32.84%
32×32	36.49%	29.56%
64×64	35.20%	28.25%
128×128	35.89%	28.82%
256×256	36.71%	29.70%

deepnet package is used. The original TMA images have a size of 1504×1440, and this immediately causes problems in running deep neural networks due to insufficient memory of the computer (the input layer has the same number of nodes as the image size). We reduce the images to a number of smaller sizes, including $16 \times 16, 32 \times 32, 64 \times 64$, 128×128 and 256×256 (popular image datasets such as the imageNet [19] uses image size of 256×256 and MNIST [45] uses 28×28). The number of layers in the deep networks we explore range from 4 to 7 (including the input and the output layer); different number of nodes for each layers are explored. Table 5 lists the best results obtained under different node size configurations that we explore for the deep neural network. For comparison, we also include results obtained by RF (on the image itself, just as the deep neural network does) under different image sizes. It can be seen that error rates achieved by deep neural networks are higher than those by RF (both higher than those achieved by *deepTacoma*). We attribute this to the small training sample size—the size of the training sample does not match the complexity of the function class for the deep neural network.

5. CONCLUSIONS

We propose to incorporate deep features in the analysis of TMA images. Such deep features can be learned in a small sample setting, which is typical of TMA images or other biomedical applications. We explore the learning of deep representations of a group nature, inspired by the success of the *cluster* assumption in semi-supervised learning and known challenges in TMA images scoring—heterogeneity and label noise. In particular, we attempt two classes of such features, clustering-based and rpTrees-based. In both cases, our experiments show that incorporating such deep features lead to a further reduction of error rate by over 6% on TACOMA for TMA images related to breast cancer. We consider this a notable improvement given that TACOMA already rivals trained pathologists in the scoring TMA images and the incremental nature of progress in this area.

Our simulations on the Gaussian mixtures provide insights on when such deep features may help. In general, we expect that deep features as we propose would help when there is label noise or when the data are heterogeneous. Note that the type of representations we have explored are of a group nature. It may be worthwhile to explore deep representations related to the geometry or topology of the underlying data, such as those revealed by manifold learning [13, 40] or topological data analysis [8, 11].

APPENDIX

In this section, we will provide more details on the algorithmic implementation of K-means clustering.

A.1 An algorithmic description of K-means clustering

Formally, given n data points, K-means clustering seeks to find a partition of K sets $S_1, S_2, ..., S_K$ such that the within-cluster sum of squares, SS_W, is minimized

$$\arg\min_{S_1,S_2,...,S_K} \sum_{i=1}^{K} \sum_{\mathbf{x}\in S_i} \|\mathbf{x} - \boldsymbol{\mu}_i\|^2, \tag{2}$$

where μ_i is the centroid of $S_i, i = 1, 2, ..., K$.

Directly solving the problem formulated as in (2) is hard, as it is an integer programming problem. Indeed it is NP-hard [1]. The K-means clustering algorithm is often referred to a popular implementation sketched as Algorithm 3 below. For more details, one can refer to [31, 47].

Algorithm 3 *K*-means clustering algorithm

1: Generate an initial set of K centroids $m_1, m_2, ..., m_K$;
2: Alternate between the following two steps
3: Assign each point x to the "closest" cluster
$$\arg\min_{j\in\{1,2,...,K\}} \|x - m_j\|^2;$$
4: Calculate the new cluster centroids
$$m_j^{new} = \frac{1}{\|S_j\|} \sum_{x\in S_j} x, \quad j = 1, 2, ..., K;$$
5: Stop when cluster assignment no longer changes.

ACKNOWLEDGEMENTS

The authors are grateful to the editor, the associate editor, and the anonymous reviewers for their constructive comments and suggestions.

Received 1 December 2017

REFERENCES

[1] Arthur, D. and Vassilvitskii, S. How slow is the K-means method? In *Proceedings of the Symposium on Computational Geometry*, pages 144–153, 2006. MR2389321

[2] Beck, A., Sangoi, A., Leung, S., Marinelli, R., Nielsen TO, T., van de Vijver, M., West, R., van de Rijn, M., and Koller, D. Systematic analysis of breast cancer morphology uncovers stromal features associated with survival. *Science Translational Medicine*, 3(108):108–113, 2011.

[3] Bentley, J. Multidimensional binary search trees used for associative searching. *Communications of the ACM*, 18(9):509–517, 1975.
[4] Bentzen, S., Buffa, F., and Wilson, G. Multiple biomarker tissue microarrays: bioinformatics and practical approaches. *Cancer and Metastasis Reviews*, 27(3):481–494, 2008.
[5] Berger, A., Davis, D., Tellez, C., Prieto, V., Gershenwald, J., Johnson, M., Rimm, D., and Bar-Eli, M. Automated quantitative analysis of activator protein-2 α subcellular expression in melanoma tissue microarrays correlates with survival prediction. *Cancer Research*, 65(23):11185, 2005.
[6] Bickel, P. J. and Levina, E. Some theory for Fisher's Linear Discriminant function, "Naive Bayes", and some alternatives when there are many more variables than observations. *Bernoulli*, 10(6):989–1010, 2004.
[7] Breiman, L. Random Forests. *Machine Learning*, 45(1):5–32, 2001.
[8] Bubenik, P. Statistical topological data analysis using persistence landscapes. *Journal of Machine Learning Research*, 16:77–102, 2015.
[9] Camp, R., Chung, G., Rimm, D., et al. Automated subcellular localization and quantification of protein expression in tissue microarrays. *Nature Medicine*, 8(11):1323–1327, 2002.
[10] Camp, R., Neumeister, V., and Rimm, D. A decade of tissue microarrays: progress in the discovery and validation of cancer biomarkers. *Journal of Clinical Oncology*, 26(34):5630–5637, 2008.
[11] Carlsson, G. Topology and data. *Bulletin of the American Mathematical Society*, 46:255–308, 2009.
[12] Caruana, R., Karampatziakis, N., and Yessenalina, A. An empirical evaluation of supervised learning in high dimensions. In *Proceedings of the Twenty-Fifth International Conference on Machine Learning (ICML)*, pages 96–103, 2008.
[13] Cayton, L. Algorithms for manifold learning. *Technical Report CS2008-0923, Department of Computer Science, UC San Diego*, 2008.
[14] Chapelle, O., Weston, J., and Schölkopf, B. Cluster kernels for semi-supervised learning. In *Advances in Neural Information Processing Systems 15*, pages 601–608, 2003.
[15] Chung, G., Kielhorn, E., and Rimm, D. Subjective differences in outcome are seen as a function of the immunohistochemical method used on a colorectal cancer tissue microarray. *Clinical Colorectal Cancer*, 1(4):237–242, 2002.
[16] Cortes, C. and Vapnik, V. N. Support-vector networks. *Machine Learning*, 20(3):273–297, 1995.
[17] Dasgupta, S. Learning mixtures of Gaussians. In *Proceedings of the 40th Annual Symposium on Foundations of Computer Science (FOCS)*, pages 634–644, 1999.
[18] Dasgupta, S. and Freund, Y. Random projection trees and low dimensional manifolds. In *Fortieth ACM Symposium on Theory of Computing (STOC)*, 2008.
[19] Deng, J., Dong, W., Socher, R., Li, L.-J., Li, K., and Li, F.-F. ImageNet: A large-scale hierarchical image database. In *IEEE Conference on Computer Vision and Pattern Recognition(CVPR)*, pages 248–255, 2009.
[20] DiVito, K. and Camp, R. Tissue microarrays–automated analysis and future directions. *Breast Cancer Online*, 8(7), 2005.
[21] Fan, J. and Fan, Y. High-Dimensional classification using features annealed independence rules. *Annals of Statistics*, 36(6):2605–2637, 2008.
[22] Freund, Y. and Schapire, R. Experiments with a new boosting algorithm. In *International Conference on Machine Learning (ICML)*, pages 148–156, 1996.
[23] Friedman, J., Bentley, J., and Finkel, R. An algorithm for finding the best matches in logarithmic expected time. *ACM Transactions on Mathematical Software*, 3(3):209–226, 1977.
[24] Gao, X., Shen, W., and Ombao, H. Regularized matrix data clustering and its application to image analysis. *arXiv:*1808.01749, 2018.
[25] Giltnane, J. and Rimm, D. Technology insight: identification of biomarkers with tissue microarray technology. *Nature Clinical Practice Oncology*, 1(2):104–111, 2004.
[26] Gong, P., Marceau, D., and Howarth, P. J. A comparison of spatial feature extraction algorithms for land-use classification with SPOT HRV data. *Remote Sensing of Environment*, 40:137–151, 1992.
[27] Goodfellow, I., Bengio, Y., and Courville, A. *Deep Learning*. The MIT Press, 2016.
[28] Gray, R. M. and Neuhoff, D. L. Quantization. *IEEE Transactions of Information Theory*, 44(6):2325–2383, 1998.
[29] Guyon, I. and Elisseeff, A. An introduction to variable and feature selection. *Journal of Machine Learning Research*, 3:1157–1182, 2003.
[30] Haralick, R. M. Statistical and structural approaches to texture. *Proceedings of IEEE*, 67(5):786–803, 1979.
[31] Hartigan, J. A. and Wong, M. A. A K-means clustering algorithm. *Applied Statistics*, 28(1):100–108, 1979.
[32] Hassan, S., Ferrario, C., Mamo, A., and Basik, M. Tissue microarrays: emerging standard for biomarker validation. *Current Opinion in Biotechnology*, 19(1):19–25, 2008.
[33] Hastie, T., Tibshirani, R., and Friedman, J. *The Elements of Statistical Learning: Data Mining, Inference, and Prediction*. Springer, 2001.
[34] Hibar, D., Kohannim, O., Stein, J., Chiang, M.-C., and Thompson, P. Multilocus genetic analysis of brain images. *Frontiers in Genetics*, 2(73):1–11, 2011.
[35] Hinton, G. and Salakhutdinov, R. Reducing the dimensionality of data with neural networks. *Science*, 313:504–507, 2006. MR2242509
[36] Holmes, S., Kapelner, A., and Lee, P. An interactive Java statistical image segmentation system: Gemident. *Journal of Statistical Software*, 30(10):1–20, 2009.
[37] Hotelling, H. Analysis of a complex of statistical variables into principal components. *Journal of Educational Psychology*, 24:417–441, 1933.
[38] Hsu, C., Ho, D., Yang, C., Lai, C., Yu, I., and Chiang, H. Interobserver reproducibility of Her-2/neu protein overexpression in invasive breast carcinoma using the DAKO HercepTest. *American Journal of Clinical Pathology*, 118(5):693–698, 2002.
[39] Hunt, W., Mark, W., and Stoll, G. Fast kd-tree construction with an adaptive error-bounded heuristic. In *IEEE Symposium on Interactive Ray Tracing*, pages 81–88, 2006.
[40] Huo, X., Ni, X., and Smith, A. A survey of manifold-based learning methods. *Recent Advances in Data Mining of Enterprise Data*, pages 691–745, 2007.
[41] Kaufman, L. and Rousseeuw, P. J. *Finding Groups in Data: An Introduction to Cluster Analysis*. Wiley, New York, 1990.
[42] Kononen, J., Bubendorf, L., Kallionimeni, A., Bärlund, M., Schraml, P., Leighton, S., Torhorst, J., Mihatsch, M., Sauter, G., and Kallionimeni, O. Tissue microarrays for high-throughput molecular profiling of tumor specimens. *Nature Medicine*, 4(7):844–847, 1998.
[43] Krizhevsky, A., Sutskever, I., and Hinton, G. E. Imagenet classification with deep convolutional neural networks. In *Advances in Neural Information Processing Systems 24*, 2012.
[44] LeCun, Y., Bengio, Y., and Hinton, G. Deep learning. *Nature*, 521:436–444, 2015.
[45] LeCun, Y., Bottou, L., Bengio, Y., and Haffner, P. Gradient-based learning applied to document recognition. *Proceedings of IEEE*, 86(11):2278–2324, 1998.
[46] Lloyd, C. D., Berberoglu, S., Curran, P. J., and Atkinson, P. M. A comparison of texture measures for the per-field classification of Mediterranean land cover. *International Journal of Remote Sensing*, 25(19):3943–3965, 2004.
[47] Lloyd, S. P. Least squares quantization in PCM. *IEEE Transactions on Information Theory*, 28(1):128–137, 1982.
[48] Marinelli, R., Montgomery, K., Liu, C., Shah, N., Prapong, W., Nitzberg, M., Zachariah, Z., Sherlock, G.,

Natkunam, Y., West, R., et al. The Stanford tissue microarray database. *Nucleic Acids Research*, 36:D871–877, 2007.
[49] Michie, D., Spiegelhalter, D. J., Taylor, C. C., and Campbell, J., editors. *Machine Learning, Neural and Statistical Classification*. Ellis Horwood, Upper Saddle River, NJ, USA, 1994.
[50] Simonyan, K. and Zisserman, A. Very deep convolutional networks for large-scale image recognition. In *Proceedings of the International Conference on Learning Repreentations*, pages 1–14, 2015.
[51] Szegedy, C., Liu, W., Jia, Y., Sermanet, P., Reed, S., Anguelov, D., Erhan, D., Vanhoucke, V., and Rabinovich, A. Going deeper with convolutions. In *Proceedings of the IEEE Conference on Computer Vision and Pattern Recognition*, 2015.
[52] Thomson, T., Hayes, M., Spinelli, J., Hilland, E., Sawrenko, C., Phillips, D., Dupuis, B., and Parker, R. HER-2/neu in breast cancer: interobserver variability and performance of immunohistochemistry with 4 antibodies compared with fluorescent in situ hybridization. *Modern Pathology*, 14(11):1079–1086, 2001.
[53] Torrey, L. and Shavlik, J. Transfer learning. *Handbook of Research on Machine Learning Applications (eds. E. Soria and J. Martin et al.)*, pages 1–22, 2009.
[54] US National Cancer Institute. https://www.cancer.gov/about-cancer/understanding/what-is-cancer.
[55] Voduc, D., Kenney, C., and Nielsen, T. Tissue microarrays in clinical oncology. *Seminars in Radiation Oncology*, 18(2):89–97, 2008.
[56] Vrolijk, H., Sloos, W., Mesker, W., Franken, P., Fodde, R., Morreau, H., and Tanke, H. Automated Acquisition of Stained Tissue Microarrays for High-Throughput Evaluation of Molecular Targets. *Journal of Molecular Diagnostics*, 5(3):160–167, 2003.
[57] Walker, R. Quantification of immunohistochemistry – issues concerning methods, utility and semiquantitative assessment I. *Histopathology*, 49(4):406–410, 2006.
[58] Wan, W. H., Fortuna, M. B., and Furmanski, P. A rapid and efficient method for testing immunohistochemical reactivity of monoclonal antibodies against multiple tissue samples simultaneously. *Journal of Immunological Methods*, 103:121–129, 1987.
[59] Ward, J. H. Hierarchical grouping to optimize an objective function. *Journal of the American Statistical Association*, 58(301):236–244, 1963.
[60] Yan, D., Bickel, P., and Gong, P. A bottom-up approach for texture modeling with application to Ikonos image classification. *Submitted*, 2017.
[61] Yan, D., Chen, A., and Jordan, M. I. Cluster Forests. *Computational Statistics and Data Analysis*, 66:178–192, 2013. MR3064033
[62] Yan, D. and Davis, G. E. The turtleback diagram for conditional probability. *The Open Journal of Statistics*, 8(4):684–705, 2018.
[63] Yan, D., Huang, L., and Jordan, M. I. Fast approximate spectral clustering. In *Proceedings of the 15th ACM SIGKDD*, pages 907–916, 2009.
[64] Yan, D., Wang, P., Knudsen, B. S., Linden, M., and Randolph, T. W. Statistical methods for tissue microarray images–algorithmic scoring and co-training. *The Annals of Applied Statistics*, 6(3):1280–1305, 2012.
[65] Yan, D., Wang, Y., Wang, J., Wang, H., and Li, Z. K-nearest neighbor search by random projection forests. In *Proceedings of the 2018 IEEE International Conference on Big Data*, 2018.
[66] Zhu, X. Semi-supervised learning literature survey. *TR 1530, Department of Computer Science, University of Wisconsin-Madison*, 2008.

Donghui Yan
Department of Mathematics
University of Massachusetts Dartmouth
MA 02747
USA
E-mail address: dyan@umassd.edu

Timothy Randolph
Fred Hutchinson Cancer Research Center
WA 98109
USA
E-mail address: trandolp@fredhutch.org

Jian Zou
Department of Mathematical Sciences
Worcester Polytechnic Institute
MA 01609
USA
E-mail address: jzou@wpi.edu

Peng Gong
Department of ESPM
University of California Berkeley
CA 94720
USA
Department of Earth System Science
Tsinghua University
China
E-mail address: penggong@berkeley.edu